Green Chemistry

PAPER

View Article Online
View Journal | View Issue

Cite this: *Green Chem.*, 2026, **28**, 4292

Accessing photocatalytically active covalent triazine-based frameworks by ball milling: a fast and facile synthesis method

Leonie Sophie Häser,[a] Sven Moos,[a,b] Felix Egger,[c] Keanu Birkelbach,[d] Mirijam Zobel,[c] Thomas Wiegand[a,b] and Regina Palkovits[*a,b,d]

Received 26th November 2025,
Accepted 5th February 2026

DOI: 10.1039/d5gc06349c

rsc.li/greenchem

Covalent Triazine-based Frameworks (CTFs) find use in a wide range of applications from gas storage to catalysis, including photocatalytic applications. While this versatility renders them a highly interesting material class, most of their synthetic protocols require either long polymerization times, high temperatures, toxic reagents, large amounts of organic solvents, or a combination of these, making current synthesis methods less attractive with regard to the green chemistry principles. We herein present a fast and facile ball milling synthesis route towards highly functionalized CTFs addressing the drawbacks of existing synthesis approaches. As a result, polymeric triazine-based structures were received within 40 min of milling time without the need for toxic chemicals or inert gas conditions. High CTF yields of more than 80% were achieved after 5 h utilizing vibrational ball milling. The sustainability of the synthesis was further improved by adjusting the salt addition to cost-effective and harmless salts. Using a photocatalytic model reaction, potential structural motives and their impact on the photocatalytic performance were elucidated.

Green foundation

1. This work introduces a rapid, solvent-free, and energy-efficient mechanochemical route for the synthesis of covalent triazine frameworks (CTFs). Triazine formation was achieved within 40 minutes of vibrational ball milling, yielding materials with small band gaps and high degrees of functionalization. Milling time was shown to strongly influence the resulting properties—including thermal stability, functional-group incorporation, and electronic structure—thereby enabling precise control without reliance on high temperatures or organic solvents.

2. The contribution to green chemistry lies in delivering a scalable and sustainable alternative to conventional solvent-based CTF syntheses. The mechanochemical approach affords superior photocatalytic performance compared to standard stCTF, driven by reduced band gaps and optimized structural motifs identified through comprehensive characterization. Importantly, the process maintains material quality while replacing Cs_2CO_3 with inexpensive, non-toxic salts, reducing both environmental impact and synthesis cost.

3. Future opportunities include a detailed milling parameter optimization, as well as expanding the scope of functional monomers suitable for this protocol and coupling mechanochemical synthesis with *in situ* monitoring to further elucidate intermediate structures. Such advances could support broader adoption of solvent-free polymerization strategies and accelerate the development of high-performance porous materials produced *via* low-waste, energy-efficient routes.

Introduction

Pathways towards a sustainable society are a central topic in research and development. One focus lies on the resilient and economical supply of energy and raw materials while significantly relieving the corresponding burden on ecosystems. The chemical industry is key to contributing to the urgently needed change by developing more sustainable processes.[1–4] High-performance materials play a crucial role in this transformation being key in *e.g.* energy technologies such as catalysts, electrodes, adsorbents or supercapacitors.[5–10] One promising material class are Covalent Triazine-based Frameworks

[a]*Institute of Technical and Macromolecular Chemistry (ITMC), RWTH Aachen University, Worringerweg 2, 52074 Aachen, Germany. E-mail: palkovits@itmc.rwth-aachen.de*
[b]*Max Planck Institute for Chemical Energy Conversion, Stiftstr. 34-36, 45470 Mülheim an der Ruhr, Germany*
[c]*Institute of Crystallography, RWTH Aachen University, Jägerstraße 17-19, 52066 Aachen, Germany*
[d]*Forschungszentrum Jülich GmbH, Institute for Sustainable Hydrogen Economy (IHE-2), An der Deutschen Welle 7a, 52428 Jülich, Germany*

(CTFs) with potential applications in gas storage, conversion and separation,[11–13] energy storage,[14–16] heterogeneous catalysis,[17–19] and photocatalytic applications.[20–23] CTFs are composed of triazine-rings which are connected *via* linker units. By choice of monomers and the linker unit, the CTF's structure and properties can be tailored. Thus, CTFs are a highly versatile material. They usually exhibit high surface areas, a high chemical and physical stability, good optoelectrical properties and a high nitrogen content.[24,25] Various synthesis methods have been developed for CTFs within the last years, ranging from the classical $ZnCl_2$-catalyzed ionothermal method,[26–28] to superacid-catalyzed approaches.[29] In addition to the monomer choice, the material characteristics also strongly depend on the chosen synthesis strategy.[30] Due to harsh reaction conditions, many synthesis protocols limit the monomer scope and often result in amorphous frameworks or partial carbonization.[31] In 2017, Wang *et al.* reported a solvothermal polycondensation reaction of diamidine-based monomers with dialdehydes in the presence of cesium carbonate and ambient air. This synthesis resulted in porous, layered CTF structures which did not show carbonization of the framework, and allowed a wide range of organic molecules to be applied as monomers resulting in a high tunability of the CTF's geometry and functionality.[32] In 2018, Liu *et al.* reported an updated synthesis using *in situ* oxidation of a dialcohol to the respective dialdehyde.[33] Despite these advances, the available synthesis strategies possess clear drawbacks such as long reaction times of several days, high reaction temperatures of 120 °C up to 600 °C, as well as an extensive need for organic solvents.[25,30] In comparison, mechanochemical methods provide efficient energy usage and reduce or even eliminate the use of organic solvents. In addition, they often shorten the synthesis time significantly to a couple of hours or even minutes.[34–38]

Despite these advantages and to the best of our knowledge, only two mechanochemical CTF syntheses have been reported so far. Troschke *et al.* presented a mechanochemical synthesis based on ball milling towards highly porous CTFs in 2017. Herein, cyanuric chloride was used as the triazine implementing unit and benzene, for example, as a monomer. Upon addition of $AlCl_3$ as the activating agent and $ZnCl_2$ as a bulking agent, porous CTFs were received within 1 h. *Via* this synthesis route, various monomers were successfully converted to CTFs.[39] However, cyanuric chloride is known for its toxic and labile character, and other reagents used were not only toxic but also highly cancerogenic. Moreover, the synthesis required argon atmosphere, making the synthesis procedure elaborate and demanding. In 2024, Hutsch *et al.* presented the first cyclotrimerization of nitriles towards CTF in the ball mill. Again, inert gas atmosphere was applied in the synthesis, as well as the super acid trifluoromethanesulfonic acid.[40]

We herein report a proof-of-concept protocol for a sustainable, efficient and straightforward mechanochemical CTF synthesis. CTF-1 is produced from terephthalimidamide dihydrochloride (**1**) and terephthalaldehyde (**2**) under the addition of cesium carbonate (Scheme 1). The presented synthesis strategy allows for a fast synthesis using less hazardous chemicals and under ambient conditions. Highly functionalized and non-carbonized CTF structures are generated within 40 min in the vibrational ball mill. Within 5 h of milling time, high conversions of over 80% are achieved. Multiple synthesis parameters are screened and their impact on the quality of the received materials quantified by employing the CTFs in the photocatalytic production of hydrogen peroxide as benchmarking reaction demonstrating auspicious photocatalytic activity. Alongside the catalytic testing, possible structural differences effecting the photocatalytic performance are elucidated.

Results and discussion

Synthesis and characterization

Inspired by the amidine-based polycondensation, CTF-1 was synthesized *via* vibrational ball milling using terephthalimidamide dihydrochloride (**1**), terephthalaldehyde (**2**), and Cs_2CO_3. All ball milling experiments were performed on a mixer mill using only hardened stainless steel milling equipment (15 mL jar, one 15 mm ball, 50 Hz). Experiments using 1,4-benzendi-

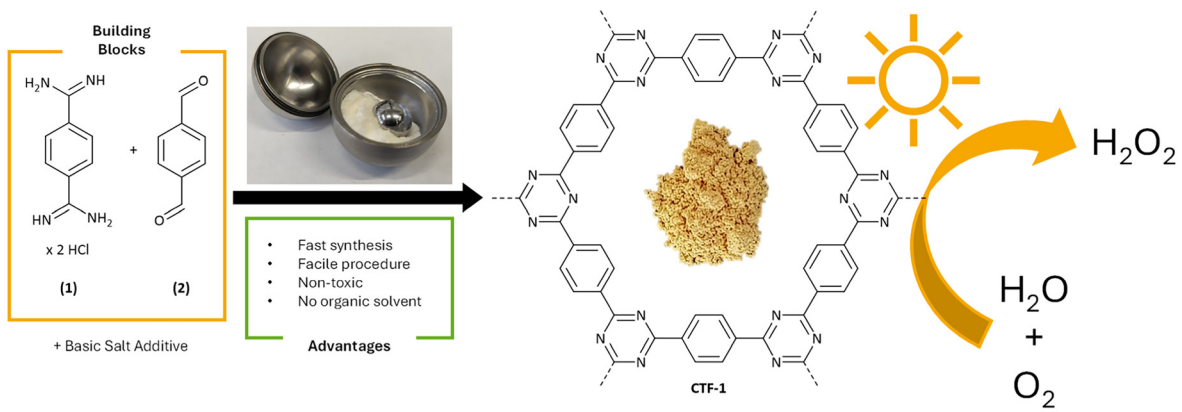

Scheme 1 Mechanochemical synthesis towards photocatalytically active CTF presented in this work and their advantages.

methanol, which enabled control of the solvothermal analogue *via in situ* oxidation, did not result in a reaction using a milling time of 5 h. In contrast, directly applying the dialdehyde as monomer resulted in the formation of a yellow powder. For further analysis of the polymerization progression upon milling the solid educts, the milling time was screened. As expected, the solid yield steadily increased from 53% after 10 min, to 81% after 5 h in the ball mill. Notably, the solid

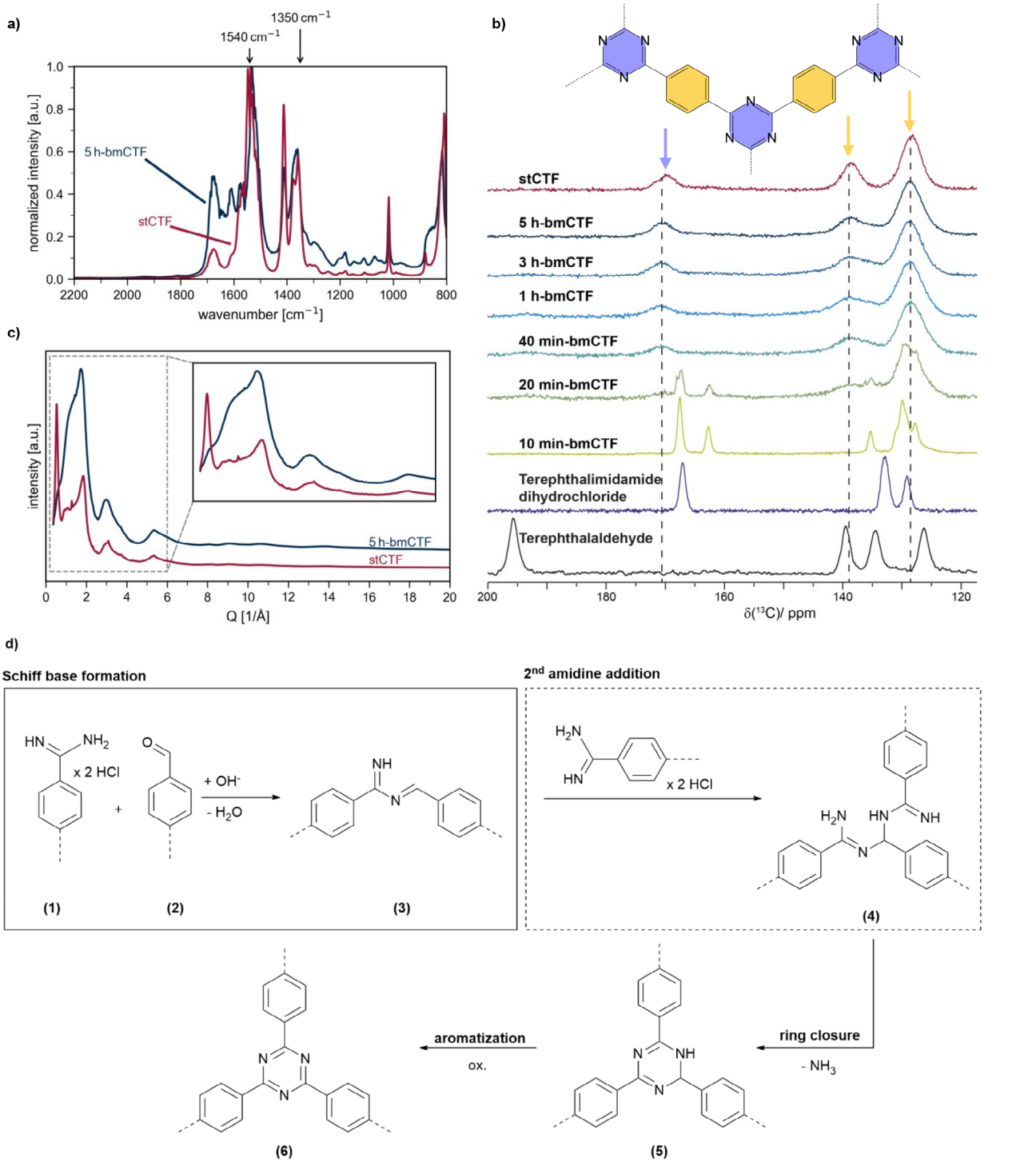

Fig. 1 (a) DRIFTS spectra of stCTF (red) and 5 h-bmCTF (blue), (b) stacked excerpts of $^{1}H-^{13}C$ CP-MAS NMR spectra of terephthalimidamide dihydrochloride (**1**) (blue), terephthalaldehyde (**2**) (black), stCTF (red) and bmCTF (green to blue) at different milling times (recorded at 16.4 T and 17.0 kHz MAS frequency), (c) PXRD data for the stCTF (red) and 5 h-bmCTF (dark blue), and (d) proposed reaction mechanism including the expected main intermediates. For the full IR and solid-state NMR spectra, as well as PXRD patterns, see Fig. S2–S5, S13 and S19.

obtained after 10 min did not show a pronounced yellow color, indicating insufficient and incomplete polymerization (Fig. S1). To allow for comparison of the new mechanochemical approach to the established procedures, the CTFs prepared *via* ball milling (bmCTFs) were compared to the solvothermal analogue (stCTF). Since the highest yield was achieved after a milling time of 5 h, the comparison focusses on 5 h-bmCTF and stCTF. Confirmation of the successful network formation and structure elucidation were achieved using Diffuse Reflectance Infrared Fourier Transform Spectroscopy (DRIFTS) experiments (Fig. 1a and Fig. S2–S5). Strong C=N vibrations at 1540 cm^{-1} and 1350 cm^{-1}, typical for the triazine rings evolving during the network formation, are observed for both CTFs.[23] These signals are expected for a successful trimerization, confirming the polycondensation towards triazines took place. For bmCTFs, these triazine signals first appear after a milling time of 20 minutes (Fig. S2). This correlates with the formation of the triazine moiety and underlines the feasibility of monitoring structural differences and thus the polymerization progress *via* DRIFTS. Interestingly, the triazine band at 1540 cm^{-1} is broadened and slightly shifted for the bmCTFs compared to the stCTF. This implies that the chemical environment of the triazine ring is slightly altered and less uniform for the bmCTF.[41,42] Accordingly, the bmCTF samples show additional signals throughout the whole spectrum at any milling time. The band at 1680 cm^{-1} is assigned to remaining amidine functionalities present in the framework. The nitrile bands at 2230 cm^{-1} are more pronounced for the bmCTFs, which are attributed to the nitrile C=N vibrations formed upon the deconstruction of amidine-functionalities.[43] As these bands are of higher intensity for bmCTFs than for the stCTF, it can be concluded that a stronger decomposition of the amidine-groups takes place in the ball mill than for the nucleation and particle growth controlled solvothermal synthesis. The bands at 1610 cm^{-1} and 1580 cm^{-1} are assigned to trimerization intermediates (Fig. 1d), such as intermediate structures after the second amidine addition reaction (**4**), or before complete aromatization to the triazine ring (**5**).[41,42] The proposed reaction mechanism will be further discussed at a later point. Compared to the stCTF, most bands are of higher intensity for the bmCTFs. Notably, all spectra are normalized to the most intense band at 1540 cm^{-1} which is assigned to the formed triazine ring. The differences in the band's intensities, therefore, need to be considered relative to the triazine rings formed, rather than to the total amount of functionalities present in the framework. We hypothesize that bmCTFs are comprised of a highly functionalized structure originating mainly from partially condensed monomers and intermediates with a smaller share originating from side reactions.

Solid-state Nuclear Magnetic Resonance (NMR) spectroscopy allows for the direct characterization of the material taken from the milling jar in an *ex situ* fashion.[44] ^{1}H–^{13}C cross-polarization (CP-) magic-angle (MAS) solid-state NMR was used to follow the structural evolution of bmCTFs during the course of the milling reaction. The corresponding spectra were compared to the respective monomers utilized in synthesis (Fig. 1b and S13).[45] Based on the immediate disappearance of the highly shifted carbonyl ^{13}C resonances at around 195 ppm, it was concluded that terephthalaldehyde (**2**) is already completely converted after very short milling times. At 10 minutes of ball milling, distinct and rather sharp resonances are observed which align only partially with the resonances of starting material (**1**), suggesting the formation of a reaction intermediate. In conjunction with the vanishing of the aldehyde signal, we propose the formation of the Schiff base (**3**) obtained after the first condensation reaction (Fig. 1d). This indicates that the first condensation reaction consuming the aldehyde functionalities is completed already within the first 10 min of ball milling. The signals broaden significantly after 20 minutes of ball milling, although a few sharp signals remain, indicating that CTF formation further evolves along larger frameworks being built, while measurable quantities of smaller scale intermediates remain during that time. It was found that these intermediates are stable for the 10 min-bmCTF, but not for the 20 min-bmCTF, indicating incomplete reaction for short milling times (Fig. S14). At milling times above 40 min, mainly the broad resonances of the formed CTFs are observed, suggesting the conversion of the intermediates to larger CTF networks. Compared to bmCTFs, the ^{13}C CP-MAS spectrum of stCTF reveals slightly narrower resonances for the peaks at 128 and 140 ppm, indicating a higher structural disorder for the bmCTF samples. Interestingly, a minor chemical-shift difference for the ^{13}C resonances of the triazine rings between the samples is observed. Although the origin of this effect remains unclear, it is in line with the analysis of the IR spectra also showing a broadening and shift of the triazine band presumably due to an altered chemical environment. A close inspection of the ^{13}C spectrum (Fig. S15) reveals additional weak resonances with chemical shift values ranging between 50 to 80 ppm pointing to sp^3 hybridized C-atoms as present in the intermediates (**4**) and (**5**) proposed for the IR bands at 1610 cm^{-1} and 1580 cm^{-1}.

Powder X-ray Diffraction (PXRD) patterns (Fig. 1c and Fig. S19) of 5 h-bmCTF and stCTF acquired at a beamline source are dominated by broad peaks and diffuse intensities. In the case of both, the 5 h-bmCTF and the stCTF, sharp Bragg peaks are entirely missing, indicating an amorphous phase to be dominating for both synthesis routes. The most noticeable difference between the two samples is the broad reflex at very low $Å^{-1}$ for the 5 h-bmCTF. In contrast, the stCTF shows a sharp peak at Q = 0.54 $Å^{-1}$, corresponding to a distance of 11.6 Å, which can be attributed to an ordered pore structure.[23] PXRD experiments conducted on a lab-scale diffractometer (Fig. S20 and S21) do not show different behavior for the different milling times. Only the 10 min-bmCTF shows crystalline reflexes, which can be explained by incomplete polymerization. Pair Distribution Function (PDF, Fig. 2a and S18) analyses provide insights into a very similar local structure for the stCTF and 5 h-bmCTF. The first three significant distances at 1.40, 2.40 and 2.84 Å indicate a similar triazine unit structure for both CTFs. The first peak can be fitted with two Gaussian functions having their center at 1.38 and 1.52 Å, being the typical bond lengths for an N–C resonant in the triazine-ring unit, and a C–C bond distance which connects to adjacent

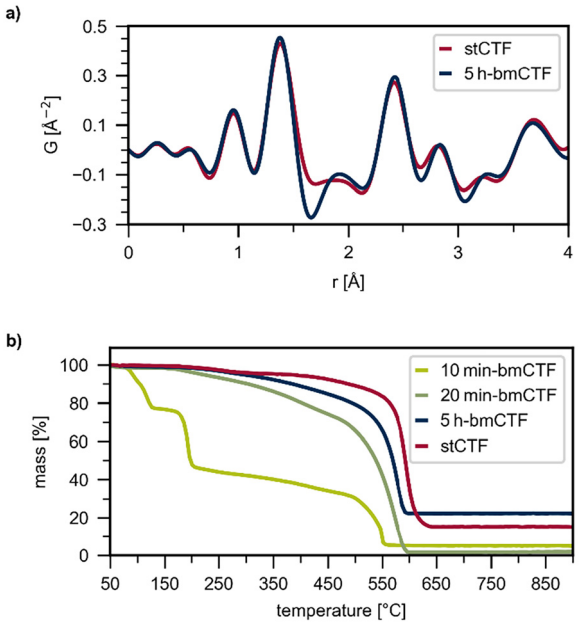

Fig. 2 (a) Section of the Pair Distribution Function (PDF) plots derived from the total scattering data for the 5 h-bmCTF (blue) and stCTF (red) samples. (b) Thermogravimetric analysis for the stCTF (red) and some of the bmCTFs (green to blue) in air atmosphere. The full plots are shown in S18 and S26.

units, respectively.[46] Neither sample shows signs of long-range order, such as stacking of the CTF sheets or homogeneous pore structures. Such structures have already been shown to be visible in the PDF as an intermediate and larger length scale sinusoidal oscillation with a wavelength corresponding to the stacking distance or pore size respectively.[47] The PDF of the stCTF shows a peak at 11 Å that could be the result of a pore diameter as mentioned earlier. However, no recurrence of this range over a long distance can be detected, suggesting a rather heterogeneous pore channel distribution.

Elemental analysis results (Table S4) are in agreement with the theoretical values for an ideal framework and with each other. This further indicates successful polymerization, as the nitrogen content is in an expected ratio with respect to the carbon content. This also highlights that carbonization, one of the main issues in CTF synthesis, does not occur during the ball milling protocol. The slightly increased hydrogen content is attributed to absorbed species and H-containing species. Additionally, ICP analysis (Table S4) was employed to test for impurities from the ball milling equipment or the synthesis. For this, the cesium, iron and chromium content were analyzed. A low cesium content for both synthesis methods confirms, that bmCTFs do not suffer from high cesium contamination. Moreover, a significant contamination caused by the stainless-steel ball milling material can also be excluded. Due to the controlled kinetics during the stCTF's synthesis, a high specific surface area (591 $m^2\ g^{-1}$) and porosity (0.201 $cm^3\ g^{-1}$) are achieved in N_2-physisorption experiments (Table S5). The stCTF also shows a pronounced microporosity (0.192 $cm^3\ g^{-1}$). In contrast, the obtained bmCTFs showed a significantly lower specific surface area (27 $m^2\ g^{-1}$ for 5 h-bmCTF), while maintaining about a quarter of the total pore volume (0.055 $cm^3\ g^{-1}$ for 5 h-bmCTF). In light of the considerable experimental errors when interpreting small specific surface areas, they are not interpreted in detail for bmCTFs. The lower pore areas of bmCTFs compared to stCTFs are attributed to a trade-off between the formation of an ideal CTF structure, effecting a lowly functionalized, high surface area network, and the presence of intermediate structures within the scaffold, resulting in a lower surface area, yet highly functionalized network. We thus propose that the polymerization in the ball mill results in a highly functionalized CTF structure containing non-condensed monomer functionalities, side-products and intermediates. These findings are additionally supported by water physisorption experiments for stCTF and 5 h-bmCTF (Fig. S23 and S24). At 0.9 p/p_0, stCTF shows a higher volume of absorbed water (301 $cm^3\ g^{-1}$) compared to the bmCTF (126 $cm^3\ g^{-1}$). Considering the much lower surface area of the bmCTF, however, the volume of absorbed water per m^2 surface is almost eight times higher for the bmCTF (3.9 mL m^{-2}) than the stCTF (0.5 mL m^{-2}). Thus, the wettability of the mechanochemical CTF is improved, likely due to its' high functionalization.

Thermal stability tests of the bmCTFs show a slow but consistent mass loss starting above 250 °C in thermogravimetric experiments under N_2-atmosphere (Fig. S25), except for 10 min-bmCTF which does not show thermal stability at temperatures higher than 75 °C. In contrast, stCTF only exhibits minimal degradation until 675 °C, at which point degradation accelerates rapidly. In air, bmCTFs undergo a slight mass loss up to 500 °C whereinafter they decompose completely (Fig. 2b and S26). bmCTFs again behave similarly except for 10 min-bmCTF, which shows significant degradation at 80 °C, 180 °C, and 500 °C. The reduced thermal stability of 10 min-bmCTF corresponds to its low connectivity and insufficient polymerization, in line with all previous findings. The stCTF possesses a relatively constant stability up to 600 °C. Additionally, differences in the morphology comparing bmCTFs with stCTF can be observed in Scanning Electron Microscopy (SEM, Fig. S29–S31) pictures. While stCTF shows a highly structured and porous surface, bmCTFs appear to be agglomerations of unstructured particles of different sizes generating a structured surface. As one key application area of non-carbonized CTFs is photocatalysis, their band gap energies were determined *via* the Tauc plot method using UV-Vis Diffuse Reflectance Spectroscopy (DRS) measurements (Table S6). While the band gap energies of both the 5 h-bmCTF (2.51 eV, 493 nm) and the stCTF (3.08 eV, 403 nm) are within the visible wavelength range, the band gap energy of the ball milled CTF is considerably lower, allowing the utilization of a much broader part of the visible light spectrum and likely translating to a significantly increased photocatalytic activity. This becomes evident again in UV-Vis absorption spectra (Fig. S32), where a strong Urbach Tail is visible for 5 h-bmCTF. In literature, the appearance of an Urbach Tail is related to the presence of many intra-band gap states, usually caused by defects or doping.[48–51] These findings

match the different colors of both materials. While the stCTF shows a typical pale-yellow color, the bmCTFs yellow coloration is much darker in comparison (Fig. S1). Considering the ball milling time, a decreasing band gap energy can be observed with longer reaction times. As after only 10 min of ball milling, when the polymer network was not fully formed, a band gap energy of 2.78 eV (446 nm) was measured already, the readily decreasing band gap energy towards 5 h-bmCTF is attributed to the extension of the covalently linked electron–π-system, which outweighs the influence of the accompanying decrease in scaffold functionality.

Finally, as a way of determining the quality of the received materials from an application viewpoint, the impact of the different synthesis strategies on the photocatalytic activity of the CTF is quantified. For this, the transformation of water to hydrogen peroxide was chosen as a benchmark reaction to showcase the CTFs general potential for photocatalytic applications.[20,52–54] The photocatalytic experiments were conducted with 0.25 mg mL^{-1} of catalyst in deionized water without the addition of sacrificial agents or pH adjustment, applying irradiation with a cool-white LED mimicking natural sunlight (1000 W m^{-2}) for 1 h. A constant flow of synthetic air (50 mL min^{-1}) was applied to ensure oxygen saturation. Under these conditions, stCTF and the 5 h-bmCTF were tested (Table S7 and Fig. S34). Confirming the previously proposed activity trends based on band gap energy and network functionality, the bmCTFs exhibites a more than fivefold increase in catalytic activity of 730 μmol g^{-1} h^{-1} compared to stCTF (135 μmol g^{-1} h^{-1}). This trend is reflected in time resolved measurements ranging from 15 min to 3 h irradiation time (Table S8 and Fig. S35). At any time, the bmCTF shows a higher activity compared to the stCTF. Moreover, the stCTFs activity drops below 100 μmol g^{-1} h^{-1} between 1 and 2 h irradiation time, while this was not the case for the bmCTF within the studied time frame. Photocatalytic experiments using LEDs at distinct different wavelengths (365 nm to 460 nm) highlight the significant impact of the materials' band gap energies on their resulting photocatalytic activity (Table S9 and Fig. S36). While the stCTF outperforms its' counterpart for irradiation at shorter wavelengths (<395 nm), the bmCTF shows relatively unchanged activity throughout the screened wavelengths. These results match the respective band gap energies of both materials, as the activity of stCTF significantly drops for wavelengths greater its' band gap energy (>405 nm). Thus, the higher activity of bmCTF at white light irradiation is strongly impacted by the red shift of its' band gap energy. It should be noted that the higher activity under white light irradiation renders the bmCTF more applicable to the direct usage of sunlight energy. Reference experiments without catalyst addition or without irradiation did not show significant hydrogen peroxide generation (Fig. S37).

The activity of metal-free organic framework photocatalysts can primarily be tuned by variation of the monomer units.[48] As such, the presented synthesis protocol immediately recommends itself for further studies on monomer structure variations. In the same way, activity is also influenced by various characteristics such as the material's polarity and thus wettability, particle size, stability, crystallinity and defects.[50] Many studies have shown that high porosity and crystallinity increase the photocatalytic activity of organic frameworks. This is usually related to the larger surface area available for substrate interaction, reduced migration distance for generated charges to the surface, as well as improved light scattering resulting in enhanced light harvesting of the photocatalyst.[55] These advantages, however, can also be achieved and therefore compensated by photocatalysts with improved hydrophilicity due to higher functionalization, or enhanced light absorption achieved by smaller band gap energies. Additionally, charge-carriers can be stabilized in defect-rich materials resulting in increased overall photocatalytic activity and mitigating the need for short charge migration distances.[51,56–58] We thus hypothesize that the bmCTFs' higher functionalization results in improved wettability, as well as a lower band gap energy increasing the bmCTFs photocatalytic activity under white light irradiation consequently.

In either case, an in depth understanding of the contained structural moieties and the individual structure evolutions and defectivities during the ball milling is highly desirable, and further investigations were carried out to obtain such.

Structural investigation

Additional reference experiments were conducted to identify the potential structural motives contained in bmCTFs to which we attribute the observed increase in photocatalytic activity. In the first set of experiments, the ratio of both monomers, the terephthalimidamide dihydrochloride (**1**), terephthalaldehyde (**2**), were varied in order to induce an increased defect density. All materials were milled for 5 h under identical conditions. In the following, the ratio of aldehyde to amidine will be displayed *via* the equivalents of amidine used in the synthesis in the index. The ideal stoichiometric ratio of 1 : 2, as used in the previous experiments, will thus be noted as $bmCTF_2$. In addition to the ratio of 1 : 2, an excess of amidine was used ($bmCTF_3$), as well as an amidine deficit ($bmCTF_1$ and $bmCTF_{1.5}$).

Solid-state NMR spectroscopy (Fig. S16) and DRIFTS measurements (Fig. 3a) confirm the formation of triazine rings for all materials. For both experiments with a sub-stoichiometric amount of amidine, a band at 1650 cm^{-1} can be assigned to the aldehyde (**2**). For $bmCTF_2$ and $bmCTF_3$, this band is not visible anymore, confirming the previously proposed, fast first condensation reaction between amidine and aldehyde to form a Schiff base (**3**). Again, DRS experiments were analyzed *via* the Tauc plot method to estimate the material's band gap energies (Table S6). All $bmCTF_x$ exhibited comparable band gap energies. Interestingly, the band gap energy of the $bmCTF_x$ with deficient amidine content showed slightly lower E_g values than $bmCTF_2$. This implies the occurrence of the intermittently formed species (**3**) as a contributor to the lowered band gap energies.

In a second reference experiment, a 5 h milled bmCTF was heated to 160 °C in DMSO for 24 h. These conditions are comparable to the last synthesis step for the stCTF, thus enabling conditions for ring closure and aromatization reactions. DRIFTS

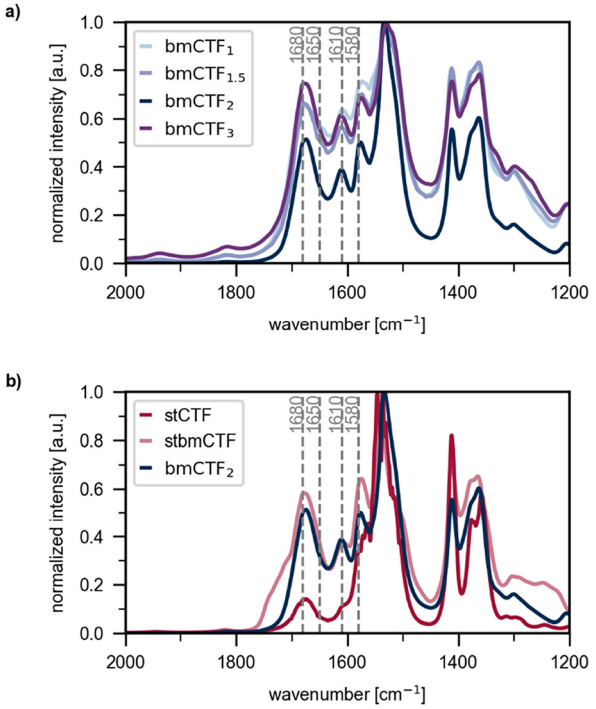

Fig. 3 (a) DRIFTS spectra of the materials synthesized applying different equivalents of the monomers. (b) DRIFTS spectra of the bmCTF$_2$ / 5 h-bmCTF (dark blue), as well as the stCTF and stbmCTF (red). Important bands at 1680, 1650, 1610, and 1580 cm^{-1} are marked with vertically dotted lines. Full spectra are shown in Fig. S8–S11.

analysis of this stbmCTF shows altered functionalities (Fig. 3b). While the triazine signals expected for a CTF structure are maintained, the band at 1610 cm^{-1} broadened compared to the analogue bmCTF (5 h-bmCTF, bmCTF$_2$). This fits the hypothesis that the band at 1680 cm^{-1} can be attributed to an intermediate structure before ring closure (**4**), which reacted further under solvothermal conditions. Notably, not only the band at 1610 cm^{-1} is broadened in the stbmCTF's spectrum. Tauc plot analysis of the DRS spectrum revealed a band gap energy of 2.40 eV, therefore being lower than that of the stCTF and all bmCTFs. This underscores the intricacy of the trade-off between the ideality of the framework, the degree of polymerization and the contained functionalities. In summary, these findings are in agreement with the previously proposed reaction mechanism (Fig. 1d). In addition, NMR and IR data indicate that the second amidine addition and the following ring closure and aromatization to give the final triazine ring require longer milling times or solvothermal reaction conditions. This explains the presence of intermediate structures within the framework and allows the postulation of likely structures for intermediates (**3**) and (**4**).

To compare the photocatalytic quality of the different ball milled materials all materials were again employed in the photocatalytic production of hydrogen peroxide (Table S7). Interestingly, the activity increased from 502 μmol g^{-1} h^{-1} (bmCTF$_1$) to 595 μmol g^{-1} h^{-1} (bmCTF$_3$) with increasing amidine content. Still, the activity of the bmCTF$_3$ is lower than of the stoichiometrically correct bmCTF$_2$. DRIFTS analysis showed that bmCTF$_1$ and bmCTF$_{1.5}$ still showed aldehyde bands. These signals are not visible for bmCTF$_2$ and bmCTF$_3$, which is in line with the proposed reaction mechanism. This allows several conclusions: first, that the presence of carbonyl functionalities is not beneficial to photocatalytic activity. Second, that the trimerization intermediates following the second amidine addition are beneficial with regard to lowering the band gap energy. Lastly, it can be concluded that multiple parameters need to be considered when designing a material for *e.g.* photocatalytic activity, such as the degree of polymerization *versus* the degree of functionalization.

Enhancing sustainability

Mechanochemical synthesis methods are known for their potential to be more sustainable compared to their solvothermal counterparts. This is commonly evaluated based on green metrics.[59–63] The presented ball milling procedure enables CTF synthesis without the need for external heating, while also offering shorter reaction times and reduced need for organic solvents. To evaluate this, a selection of green metrics was calculated for both, the bmCTF and stCTF synthesis procedures (Table 1). While a smaller environmental factor (*E*-factor) and process mass intensity (PMI) are calculated for the bmCTF, these values improve further drastically upon excluding water from these calculations. This can be attributed to water as the main contributor to the solvent usage of the mechanochemical synthesis. As a result, the *E*-factor of bmCTF excluding water is about 7-times smaller than the *E*-factor of its' solvothermal analogue. Additionally, an estimation of energy consumption for both synthesis methods indicate that the ball milling synthesis is far more sustainable, requiring less than 1% of the energy input needed for stCTF synthesis.

To further improve the sustainability of the new ball milling synthesis, a variation of the salt additive was performed. In comparison to other carbonates, Cs_2CO_3 suffers from high costs and hazardous properties. Hence, additional experiments applying K_2CO_3 (K-bmCTF) to test the exchangeability of the carbonate were conducted. To further investigate whether the carbonate functionality is needed or if any basic salt can be applied, Na_3PO_4 (P-bmCTF) and NaCl (N-bmCTF) were also tested. The usage of NaCl as an inert grinding additive can potentially result in a templating effect, increasing the surface area and pore volume of the resulting polymer.[64]

Table 1 Selection of green metrics calculated for the synthesis of 5 h-bmCTF and stCTF

Green metrics	stCTF	bmCTF
Energy input	49.5 kWh	0.35 kWh
Reaction time	60 h	5 h
Solvent usage (incl. water)	266 mL	120 mL
Solvent usage (excl. water)	209 mL	30 mL
PMI (incl. water)	454	247
PMI (excl. water)	353	56
E-factor (incl. water)	452	246
E-factor (excl. water)	351	54

Hence, a mixture of K_2CO_3 and NaCl (KN-bmCTF) was also applied in the ball milling synthesis. For all salt variation tests, the amount of salt added was kept constant with regard to molarity of base added in the Cs_2CO_3 reaction (C-bmCTF) in order to ensure comparability of the different bases. It should be noted that different masses of salt were thus added, which can also have an impact on ball milling reactions. Based on the previously discussed results, a milling time of 5 h was applied to all additive variation experiments.

Independent of the basic salt added, a non-soluble and yellow-colored solid was obtained within the milling time. For the N-bmCTF, however, no formation of an insoluble solid was achieved. It can thus be concluded that a basic salt is needed for successful polymerization, as it is required for the activation of the monomer functionalities.

Structure elucidation was again performed using DRIFTS experiments (Fig. 4). The typical triazine bands at 1500 cm^{-1} and 1350 cm^{-1} are observed for all CTFs, proving a successful synthesis. The replacement of Cs_2CO_3 in the synthesis is therefore possible, enabling a further improved sustainability of this ball milling synthesis compared to other synthesis procedures reported in literature. For the carbonate-based K-bmCTF, KN-bmCTF and C-bmCTF, the spectra are similar both qualitatively and regarding signal intensities. Therefore, the polymerization progression and functionalities present do not depend significantly on the type of carbonate, but rather the milling time. Solid-state NMR spectra (Fig. S17) also show that the use of different carbonates has no significant impact on the CTF structure, since the ^{13}C CP-MAS spectra are highly similar. Only the synthesis employing sodium phosphate results in additional resonances around 165 ppm. Thermogravimetric analyses in both N_2-atmosphere and under air (Fig. S27 and S28) confirm similar properties of the CTFs independent of the salt additive chosen. PXRD analyses (Fig. S19 and S22) of KN-CTF and K-bmCTF are in good agreement to the one of 5 h-bmCTF, with no sharp Bragg peaks visible. For the P-bmCTF, the presence of sharp reflexes suggests residual crystalline impurities within the framework's structure. PDF data (Fig. S18) as well indicate the same local structure, leading to the conclusion that the variation in carbonate additives results in the formation of a similar triazine framework structure as for 5 h-bmCTF and stCTF, respectively. As for the milling time variation, a low-porous character and low surface area are obtained (Table S5). Using SEM (Fig. S29–S31), no major differences can be observed for the CTF morphologies. The Tauc plot analysis based on UV-Vis DRS (Table S6) and the UV-Vis absorption spectra (Fig. S33) confirm similar band gap energies and absorption behavior for all CTF. While the obtained band gap for the carbonate based CTFs are within 2.51 eV to 2.57 eV, P-bmCTF shows a slightly lower band gap energy of 2.43 eV. All bmCTFs were again tested in the photocatalytic production of hydrogen peroxide (Table S7). Compared to the stCTF, all bmCTF exhibited a significantly higher activity, with the lowest activity for P-bmCTF (471 μmol g^{-1} h^{-1}) and the highest still for C-bmCTF (730 μmol g^{-1} h^{-1}). Notably, the differences in band gap energy are not reflected in the photocatalytic activities, stressing that the production of hydrogen peroxide seems to be influenced by multiple interconnected factors along with the band gap energy and network functionality.

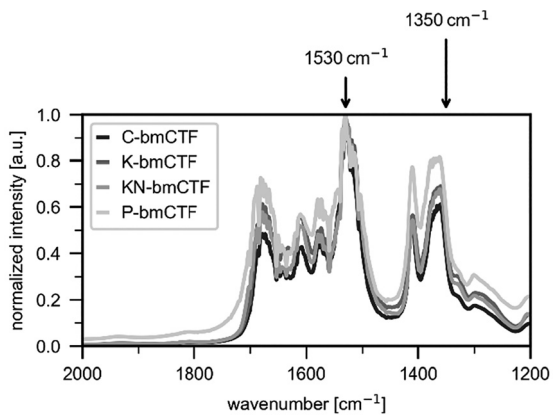

Fig. 4 DRIFTS results of the bmCTFs using different basic salt additives. The previously denoted 5 h-bmCTF is referred to as C-bmCTF. Full spectra are shown in Fig. S6 and S7.

Conclusion

In this work, we demonstrated a novel, fast and green synthesis of CTFs in a vibrational ball mill. It was possible to confirm the formation of triazine units within 40 minutes. Further unique properties, such as small band gap energies and high functionalization, were detected. A milling time investigation proved to be influential towards the resulting properties, such as thermal stability, as well as the amount and nature of functionalities. Increasing the milling times also improved yields and resulted in lower band gap energies. The latter facilitate superior photocatalytic activity at white light irradiation compared to the literature-known stCTF, hence emphasizing the potential of this synthetic protocol. Further structural investigations allowed the identification of the most likely intermediate structures originating from the ball milling protocol. Similarly, it was possible to correlate the inclusion of several structural motives and their impact on the properties of their respective CTFs. In addition to the fast and solvent-free character of the presented new mechanochemical CTF synthesis, we demonstrated the ability to further improve sustainability aspects and lower synthesis costs upon substitution of Cs_2CO_3 for non-toxic and inexpensive salts. Thereby, yield, structure, stability and small band gap energies were maintained for the CTFs.

The presented synthesis serves as a proof-of-concept study. Milling parameters, such as milling ball diameter and number, milling material, liquid assisted grinding (LAG), and frequency, should be revised in future studies. Upon optimization, the mechanochemical synthesis of CTF bears potential for further improvements in material properties and photocatalytic activity.

To summarize, the presented synthesis method enables the fast and solvent-free synthesis of highly functionalized CTF

stressing the importance of looking beyond the scope of solvent-based synthesis strategies.

Author contributions

L. S. Häser: conceptualization, data curation, formal analysis, investigation, visualization, writing of the original draft; S. Moos: formal analysis, investigation, visualization, writing of the original draft; F. Egger: formal analysis, investigation, writing of the original draft; K. Birkelbach: formal analysis, reviewing and editing; M. Zobel: funding acquisition, supervision, reviewing and editing; T. Wiegand: funding acquisition, supervision, reviewing and editing; R. Palkovits: conceptualization, funding acquisition, supervision, reviewing and editing.

Conflicts of interest

There are no conflicts to declare.

Data availability

The data supporting this study have been made available at Zenodo (10.5281/zenodo.18600035) and in Supplementary Information (SI). See DOI: https://doi.org/10.1039/d5gc06349c

Ref. 65–70 are cited in the SI.

Acknowledgements

The authors acknowledge the Fuel Science Center (EXC 3782186, ID: 390919832) funded by the Excellence Initiative of the German federal and state governments. We also acknowledge beamtime at beamline I15-1 at Diamond Light Source (Didcot, England), proposal CY29917 and local support by Phil Chater. L. S. H. gratefully thanks the German Federal Environmental Foundation for financial support. T. W. acknowledges support from the Deutsche Forschungsgemeinschaft (DFG, German Research Foundation, Heisenberg fellowship, project number 455238107) and the Max Planck Society. The authors acknowledge the funding by the German Federal Ministry of Education and Research (BMBF) and the Ministry of Economic Affairs, Industry, Climate Action and Energy of the State of North Rhine-Westphalia through the project HC-H2. Open Access funding provided by the Max Planck Society.

References

1 M. S. Prévot, V. Finelli, X. Carrier, G. Deplano, M. Cavallo, E. A. Quadrelli, J. Michel, M.-H. Pietraru, C. Camp, G. Forghieri, A. Gagliardi, S. Seidel, A. Missemer, B. Reuillard, B. Centrella, S. Bordiga, M. G. Salamanca González, V. Artero, K. V. A. Birkelbach and N. von Wolff, *Chem. Sci.*, 2024, **15**, 9054–9086.
2 J. B. Zimmerman, P. T. Anastas, H. C. Erythropel and W. Leitner, *Science*, 2020, **367**, 397–400.
3 M. Farghali, A. I. Osman, I. M. A. Mohamed, Z. Chen, L. Chen, I. Ihara, P.-S. Yap and D. W. Rooney, *Environ. Chem. Lett.*, 2023, **21**, 2003–2039.
4 J. Wang and W. Azam, *Geosci. Front.*, 2024, **15**, 101757.
5 S. Lu, H. Hu, H. Sun, F. Yang, H. Zhu, M. Du, Y. Jin and W. Zhang, *Green Chem.*, 2024, **26**, 5744–5769.
6 C.-J. Na, M.-J. Yoo, D. C. Tsang, H. W. Kim and K.-H. Kim, *J. Hazard. Mater.*, 2019, **366**, 452–465.
7 H. Huang and K. Wang, *Green Chem.*, 2023, **25**, 9167–9174.
8 W. Zhang, C. Xu, C. Ma, G. Li, Y. Wang, K. Zhang, F. Li, C. Liu, H.-M. Cheng, Y. Du, N. Tang and W. Ren, *Adv. Mater.*, 2017, **29**, 1701677.
9 S. Ge, K. Wei, W. Peng, R. Huang, E. Akinlabi, H. Xia, M. W. Shahzad, X. Zhang, B. B. Xu and J. Jiang, *Chem. Soc. Rev.*, 2024, **53**, 11259–11302.
10 J. Qiu, H. Wang, Y. Zhao, P. Guan, Z. Li, H. Zhang, H. Gao, S. Zhang and J. Wang, *Green Chem.*, 2020, **22**, 2605–2612.
11 S. Bügel, A. Spieß and C. Janiak, *Microporous Mesoporous Mater.*, 2021, **316**, 110941.
12 S. Hug, M. B. Mesch, H. Oh, N. Popp, M. Hirscher, J. Senker and B. V. Lotsch, *J. Mater. Chem. A*, 2014, **2**, 5928–5936.
13 Y. Guan, B. Wang, Y.-L. Ying, P. Li and Z.-H. Zhang, *Green Chem.*, 2025, **27**, 9165–9177.
14 X. Yan, G. Zhao, C. Wu, Y. Dai, J. Xiong, X. Wang, H. Yu, Z. Wang, R. Li, J. Liu, M. Hu and J. Yang, *Green Chem.*, 2024, **26**, 10593–10603.
15 P. Xiong, S. Zhang, R. Wang, L. Zhang, Q. Ma, X. Ren, Y. Gao, Z. Wang, Z. Guo and C. Zhang, *Energy Environ. Sci.*, 2023, **16**, 3181–3213.
16 Y. Li, S. Zheng, X. Liu, P. Li, L. Sun, R. Yang, S. Wang, Z.-S. Wu, X. Bao and W.-Q. Deng, *Angew. Chem.*, 2018, **130**, 8124–8128.
17 L. Zhao, S. Shi, M. Liu, G. Zhu, M. Wang, W. Du, J. Gao and J. Xu, *Green Chem.*, 2018, **20**, 1270–1279.
18 M. Gao, J. Kou, M. Xu, K. Yuan, M. Li and Z. Dong, *Green Chem.*, 2024, **26**, 3884–3902.
19 A. Iemhoff, M. Vennewald and R. Palkovits, *Angew. Chem., Int. Ed.*, 2023, **62**, e202212015.
20 L. Li, X. Yao, W. Ou, J. Chai, R. Ma, C. Ran, A. Ma, X. Shi, P. Wei, H. Dong, H. Zhou, W. Yang, H.-C. Hu, J.-F. Wu, H. Peng and G. Ma, *Green Chem.*, 2025, **27**, 9144–9152.
21 Y. Chen, H. Chen, J. Jiang and H. Ji, *Green Chem.*, 2025, **27**, 1430–1439.
22 W. Wu, M. Chen, C. Feng, W. Li, T. Zhang, C. Zeng, B. Wang, L. Zhong and C. Dai, *Green Chem.*, 2025, **27**, 2766–2775.
23 D. Ditz, N. M. Sackers, F. Müller, M. Zobel, S. Bergwinkl, P. Nuernberger, L. S. Häser, S. Brettschneider, F. M. Wisser, C. Bannwarth and R. Palkovits, *Green Chem.*, 2024, **26**, 3397–3405.
24 S. Pourebrahimi and M. Pirooz, *Clean. Chem. Eng.*, 2022, **2**, 100012.

25 R. Sun and B. Tan, *Chem. – Eur. J.*, 2022, **29**, e202203077.
26 P. Kuhn, M. Antonietti and A. Thomas, *Angew. Chem., Int. Ed.*, 2008, **47**, 3450–3453.
27 P. Kuhn, A. Forget, D. Su, A. Thomas and M. Antonietti, *J. Am. Chem. Soc.*, 2008, **130**, 13333–13337.
28 Z.-A. Lan, M. Wu, Z. Fang, Y. Zhang, X. Chen, G. Zhang and X. Wang, *Angew. Chem., Int. Ed.*, 2022, **61**, e202201482.
29 S. Ren, M. J. Bojdys, R. Dawson, A. Laybourn, Y. Z. Khimyak, D. J. Adams and A. I. Cooper, *Adv. Mater.*, 2012, **24**, 2357–2361.
30 L. Liao, M. Li, Y. Yin, J. Chen, Q. Zhong, R. Du, S. Liu, Y. He, W. Fu and F. Zeng, *ACS Omega*, 2023, **8**, 4527–4542.
31 A. Iemhoff, J. Deischter, S. Jung, G. Tuci, G. Giambastiani and R. Palkovits, *J. Mater. Chem. A*, 2021, **9**, 5390–5403.
32 K. Wang, L.-M. Yang, X. Wang, L. Guo, G. Cheng, C. Zhang, S. Jin, B. Tan and A. Cooper, *Angew. Chem., Int. Ed.*, 2017, **56**, 14149–14153.
33 M. Liu, Q. Huang, S. Wang, Z. Li, B. Li, S. Jin and B. Tan, *Angew. Chem., Int. Ed.*, 2018, **57**, 11968–11972.
34 K. J. Ardila-Fierro and J. G. Hernández, *ChemSusChem*, 2021, **14**, 2145–2162.
35 N. Fantozzi, J.-N. Volle, A. Porcheddu, D. Virieux, F. García and E. Colacino, *Chem. Soc. Rev.*, 2023, **52**, 6680–6714.
36 I. N. Egorov, S. Santra, D. S. Kopchuk, I. S. Kovalev, G. V. Zyryanov, A. Majee, B. C. Ranu, V. L. Rusinov and O. N. Chupakhin, *Green Chem.*, 2020, **22**, 302–315.
37 B. R. Naidu, T. Sruthi, R. Mitty and K. Venkateswarlu, *Green Chem.*, 2023, **25**, 6120–6148.
38 N. Brown, Z. Alsudairy, R. Behera, F. Akram, K. Chen, K. Smith-Petty, B. Motley, S. Williams, W. Huang, C. Ingram and X. Li, *Green Chem.*, 2023, **25**, 6287–6296.
39 E. Troschke, S. Grätz, T. Lübken and L. Borchardt, *Angew. Chem., Int. Ed.*, 2017, **56**, 6859–6863.
40 S. Hutsch, A. Leonard, S. Grätz, M. V. Höfler, T. Gutmann and L. Borchardt, *Angew. Chem., Int. Ed.*, 2024, **63**, e202403649.
41 M. El-Azazy, K. Al-Saad and A. S. El-Shafie, *Infrared Spectroscopy - Perspectives and Applications*, IntechOpen, 2023.
42 B. H. Stuart, *Infrared Spectroscopy: Fundamentals and Applications*, Wiley, 2004.
43 J. Andrés, A. Beltran, M. Carda, J. Krechl, J. Monterde and E. Silla, *J. Mol. Struct.:THEOCHEM*, 1992, **254**, 465–472.
44 I. D. A. Silva, E. Bartalucci, C. Bolm and T. Wiegand, *Adv. Mater.*, 2023, **35**, 2304092.
45 S. L. James, C. J. Adams, C. Bolm, D. Braga, P. Collier, T. Friščić, F. Grepioni, K. D. M. Harris, G. Hyett, W. Jones, A. Krebs, J. Mack, L. Maini, A. G. Orpen, I. P. Parkin, W. C. Shearouse, J. W. Steed and D. C. Waddell, *Chem. Soc. Rev.*, 2012, **41**, 413–447.
46 B. He and H. Zhou, *ACS Omega*, 2020, **5**, 11618–11628.
47 A. M. Pütz, M. W. Terban, S. Bette, F. Haase, R. E. Dinnebier and B. V. Lotsch, *Chem. Sci.*, 2020, **11**, 12647–12654.
48 Y. Zhao, K. Zhang, K. Zhu, Y. Zhao, H. Zhai and J. Qiu, *Green Chem.*, 2024, **26**, 2645–2652.
49 H. Li, B. Cheng, J. Xu, J. Yu and S. Cao, *EES Catal.*, 2024, **2**, 411–447.
50 A. Rajan, M. D. Dhileepan, S. Kamalakannan, M. Prakash, S. Krishnamurthy and B. Neppolian, *ACS Appl. Energy Mater.*, 2023, **6**, 9207–9217.
51 Z. Zafar, S. Yi, J. Li, C. Li, Y. Zhu, A. Zada, W. Yao, Z. Liu and X. Yue, *Energy Environ. Mater.*, 2022, **5**, 68–114.
52 C. Krishnaraj, H. S. Jena, L. Bourda, A. Laemont, P. Pachfule, J. Roeser, C. V. Chandran, S. Borgmans, S. M. J. Rogge, K. Leus, C. V. Stevens, J. A. Martens, V. van Speybroeck, E. Breynaert, A. Thomas and P. van der Voort, *J. Am. Chem. Soc.*, 2020, **142**, 20107–20116.
53 R. Sun, X. Yang, X. Hu, Y. Guo, Y. Zhang, C. Shu, X. Yang, H. Gao, X. Wang, I. Hussain and B. Tan, *Angew. Chem., Int. Ed.*, 2024, e202416350.
54 L. Yang, Q. Wang, W. Wang, Y. Xu, L. Guo, L. Liao, Z. Li, X. Wang and W. Zhou, *Chem. – Asian J.*, 2025, **20**, e00834.
55 T. Wang, B. Tian, B. Han, D. Ma, M. Sun, A. Hanif, D. Xia and J. Shang, *Energy Environ. Mater.*, 2022, **5**, 711–730.
56 J. Liu, N. Tian, S. Ren, Z. Zhang, Z. Yang, Y. Xue, Y. Zhang, L. Gao and H. Huang, *Adv. Funct. Mater.*, 2025, **35**, 2413406.
57 R. S. Sprick, Y. Bai, A. A. Y. Guilbert, M. Zbiri, C. M. Aitchison, L. Wilbraham, Y. Yan, D. J. Woods, M. A. Zwijnenburg and A. I. Cooper, *Chem. Mater.*, 2019, **31**, 305–313.
58 Y. Kang, Y. Yang, L.-C. Yin, X. Kang, G. Liu and H.-M. Cheng, *Adv. Mater.*, 2015, **27**, 4572–4577.
59 K. Hiroishi, H. Matsumoto, H. Kasai, M. Nagao, E. Nishibori and Y. Miura, *Green Chem.*, 2026, DOI: 10.1039/D5GC05291B.
60 V. Valsamidou, S. Patra, B. Kadriu, M. G. Metzger, L. Gremaud and D. Katayev, *Green Chem.*, 2025, **27**, 7122–7128.
61 C. van Poucke, A. Vandeputte, S. Mangelinckx and C. V. Stevens, *Green Chem.*, 2023, **25**, 4271–4281.
62 J. Wang, L. Zhou, S. Liu, Z. Deng, Z. Cao and P. Li, *Powder Technol.*, 2025, **454**, 120716.
63 A. Kiani, N. Sozio and M. R. Acocella, *Mol. Syst. Des. Eng.*, 2023, **8**, 942–949.
64 P. Makuła, M. Pacia and W. Macyk, *J. Phys. Chem. Lett.*, 2018, **9**, 6814–6817.
65 S. Hediger, B. H. Meier and R. R. Ernst, *Chem. Phys. Lett.*, 1995, **240**, 449–456.
66 S. Hediger, B. H. Meier, N. D. Kurur, G. Bodenhausen and R. R. Ernst, *Chem. Phys. Lett.*, 1994, **223**, 283–288.
67 J. Filik, A. W. Ashton, P. C. Y. Chang, P. A. Chater, S. J. Day, M. Drakopoulos, M. W. Gerring, M. L. Hart, O. V. Magdysyuk, S. Michalik, A. Smith, C. C. Tang, N. J. Terrill, M. T. Wharmby and H. Wilhelm, *J. Appl. Crystallogr.*, 2017, **50**, 959–966.
68 T. Egami and S. J. Billinge, *Underneath the Bragg peaks: structural analysis of complex*, Pergamon, Amsterdam, 2nd edn, 2012.
69 S. J. L. Billinge, in *International Tables for Crystallography*, 2019, vol. H, pp. 649–672.
70 P. Juhás, T. Davis, C. L. Farrow and S. J. L. Billinge, *J. Appl. Crystallogr.*, 2013, **46**, 560–566.